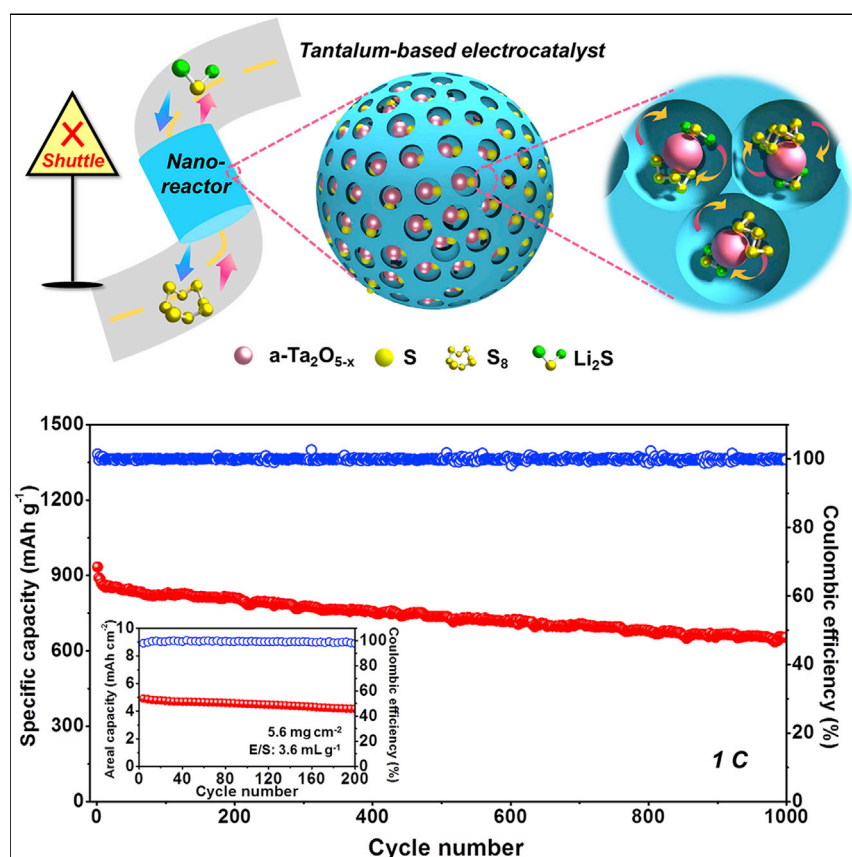


Article

Tantalum-Based Electrocatalyst for Polysulfide Catalysis and Retention for High-Performance Lithium-Sulfur Batteries



A new tantalum-based electrocatalyst for the lithium-sulfur system is developed to overcome some key challenges in lithium-sulfur batteries. Efficient crystallinity tuning is realized via a pore-constriction mechanism in the "ship in a bottle" nanostructure, which offers abundant polysulfide-retaining and catalytically active sites. Oxygen vacancies in tantalum oxide manipulating electron structure with increased intrinsic conductivity function as catalytic centers to accelerate sulfur redox reactions. Excellent rate capability and cycling stability are achieved at practically relevant sulfur loadings and electrolyte content.

Zhen Zhang, Dan Luo, Gaoran Li, ..., Jingde Li, Aiping Yu, Zhongwei Chen

zhwchen@uwaterloo.ca

HIGHLIGHTS

First application of tantalum-based materials as electrocatalyst in Li-S batteries

A pore-constriction mechanism realizes the crystallinity tuning of materials

Oxygen defects in $\text{Ta}_2\text{O}_{5-x}$ act as catalytic centers promoting polysulfide conversion

"Ship in a bottle" nanostructure design enhances catalytic activity and stability



Improvement

Enhanced performance with innovative design or material control

Zhang et al., Matter 3, 1–15
September 2, 2020 © 2020 Elsevier Inc.
<https://doi.org/10.1016/j.matt.2020.06.002>

Article

Tantalum-Based Electrocatalyst for Polysulfide Catalysis and Retention for High-Performance Lithium-Sulfur Batteries

Zhen Zhang,^{1,4} Dan Luo,^{1,4} Gaoran Li,¹ Rui Gao,¹ Matthew Li,¹ Shuang Li,¹ Lei Zhao,¹ Haozhen Dou,¹ Guobin Wen,¹ Serubbabel Sy,¹ Yongfeng Hu,² Jingde Li,³ Aiping Yu,¹ and Zhongwei Chen^{1,5,*}

SUMMARY

Polysulfide retention and catalysis are currently among the most important factors toward solving much of the technical challenges of lithium-sulfur (Li-S) batteries. Taking advantage of the electronic structure specific to tantalum, we explore the application of amorphous tantalum oxide with oxygen vacancies embedded inside a microporous carbon matrix as an electrocatalyst for the Li-S system. Through a pore-constriction mechanism, the dimensions of tantalum oxide are controlled to be nanosized with abundant polysulfide-retaining and catalytically active sites. High cycle and rate performances were achieved at practically relevant sulfur loadings and electrolyte content. We believe our identification of tantalum as a new catalyst material for Li-S batteries will incite more investigation into the specific selection of transition metals based on their electronic structures. Meanwhile, the “ship in a bottle” strategy will enlighten the structure design for energy conversion and storage systems.

INTRODUCTION

The burgeoning energy demand of modern society has been spurring extensive research interests in pursuit of next-generation high-energy-density energy-storage systems.^{1,2} Lithium-sulfur (Li-S) batteries present one of the most promising solutions to high-efficiency and cost-effective energy storage.^{3,4} Yet, despite their intriguing merits including high energy density and low cost, progress toward the widespread commercialization of Li-S batteries is impeded by several technical challenges. The intrinsic poor electrical conductivity of sulfur and discharge products ($\text{Li}_2\text{S}/\text{Li}_2\text{S}_2$), the shuttling behavior derived from the dissolution of lithium polysulfide (LPS), and, more importantly, the sluggish kinetics for LPS conversion reactions, result in poor sulfur utilization, rapid capacity decay, and unsatisfactory cycle life.^{5,6} Strategies to address these issues rely mostly on the following. (1) A well-designed electrode structure is expected to effectively retain LPS to suppress the shuttling effect and mitigate the S volume expansion during lithiation for enhanced cycle stability.^{7,8} (2) Besides, the establishment of a pass-through system enables fast electron and ion conduction for sufficient LPS redox reactions.^{9,10} (3) More importantly, an efficient electrocatalyst, such as transition metal oxides and sulfides,^{11–13} accelerates the reaction kinetics of soluble LPS conversion into insoluble $\text{Li}_2\text{S}/\text{Li}_2\text{S}_2$ to reduce their dissolution and diffusion in the electrolyte. This could promote both sulfur utilization and battery cycle life. Additionally, the catalytic activity for a reaction is correlated with the exposed active sites that have unique chemical and electronic structures.^{14,15} Defect engineering and crystallinity tuning, which

Progress and Potential

Lithium-sulfur (Li-S) batteries represent one of the most promising contenders in the “beyond lithium-ion batteries” energy-storage arena to support the ever-expanding electrical market. However, the practical application of Li-S batteries is still discouraged from several issues on the cathode side including the polysulfide shuttling behavior, sluggish sulfur redox kinetics, and volume variation during battery operation. This work presents a potent strategy to solve these challenges by developing a new tantalum-based electrocatalyst for the Li-S system. The “ship in a bottle” nanostructure of electrocatalyst featuring efficient crystallinity tuning and tailored oxygen defects enables a superior catalytic activity and stability for sulfur redox reactions, which lead to a significant increase in Li-S battery performance at practically relevant sulfur loadings and electrolyte content.

possess good capability of altering the electronic environment for enhanced LPS adsorptive and catalytic features,^{16,17} provide a promising approach to improving Li-S electrochemistry.

In the search for an efficient electrocatalyst for LPS conversion in the Li-S system, tantalum oxide (Ta_2O_5) is found to be an attractive candidate. Ta_2O_5 possesses high thermodynamic stability due to the strong Ta–O bonding, and a high dielectric constant.¹⁸ The synergism between the Ta d-orbital and the unsaturated O atom results in an effective d-band structure,¹⁹ potentially imparting catalytic characteristics with suitable valence band maximum and conduction band minimum (CBM) straddling the polysulfide redox potentials. Besides, the introduction of surface defects is capable of further tailoring band structure toward desirable electron mobility and catalytic activity.²⁰ Here, we provide the first rational application of amorphous oxygen-defective $\text{Ta}_2\text{O}_{5-x}$ as an electrocatalyst in Li-S batteries. Ultrafine $\text{Ta}_2\text{O}_{5-x}$ nanoclusters are implanted within the micropores of carbon nanospheres (a- $\text{Ta}_2\text{O}_{5-x}$ /MCN). The elaborate design presents multiple merits to fulfill the aforementioned rules. (1) The $\text{Ta}_2\text{O}_{5-x}$ -in-pore strategy presents a “ship in a bottle” structure, shaping a three-dimensional (3D) conductive nanoreactor, which not only guarantees a high surface-to-volume ratio to offer abundant polysulfide-retaining and catalytically active sites but also prevents the agglomeration of nanoclusters during synthesis and catalysis, potentially addressing the long-term issue of nanocatalyst stability. (2) The interconnected porous conductive network promotes the penetration of electrolytes and charge transfer, leading to fast motion of ions and electrons throughout the framework. (3) The tailored pitaya-like architecture promotes sulfur homogenization and buffers their volume expansion during cycling. (4) The nucleation process of $\text{Ta}_2\text{O}_{5-x}$ nanoseeds is constrained by the nanopores to realize crystallinity tuning, which alters the Ta–O bond length and provides increased binding energy (BE) between $\text{Ta}_2\text{O}_{5-x}$ and LPS. (5) Oxygen deficiencies in the Ta_2O_5 nanoclusters manipulate the local coordination environment and electron band structure, which significantly ameliorate the intrinsic conductivity and function as catalytic centers to accelerate LPS conversion. *Ex situ* X-ray absorption spectroscopy (XAS) and theoretical calculations demonstrate the enhanced LPS-retaining and electrocatalytic features driven by pore-guided amorphous structure and oxygen defects. The a- $\text{Ta}_2\text{O}_{5-x}$ /MCN-based sulfur electrode presents excellent Li-S performance, i.e., superb rate capability up to 5 C, long-term cyclability over 1,000 cycles with an ultra-low capacity fading rate of 0.029% per cycle, and high areal capacity of 5 mAh cm⁻² under raised sulfur loading of 5.6 mg cm⁻² and lean electrolyte/sulfur ratio of 3.6 mL g⁻¹.

RESULTS AND DISCUSSION

The synthesis strategy of a- $\text{Ta}_2\text{O}_{5-x}$ /MCN is illustrated in Figure 1A. The initial microporous carbon nanosphere, MCN, was prepared by a unique dual-activation technique involving chemical and physical activation simultaneously (Figure S1). MCN presents regular sphericity with a uniform diameter of 150 nm (Figure S2). By means of a wet-impregnation strategy, MCNs were immersed in tantalum(V) chloride ethanol solution to lead the built-in implantation of tantalum-alcoholysis product inside pores of MCN (denoted as $\text{Ta}(\text{OC}_2\text{H}_5)_x/\text{MCN}$).²¹ Following this, the Ta^{5+} -impregnated MCN was pyrolyzed in the H_2 atmosphere, in which amorphous tantalum oxide with rich oxygen vacancies is shaped and immobilized within the pores (a- $\text{Ta}_2\text{O}_{5-x}$ /MCN). Figure S3 displays the typical scanning electron microscopy image of a- $\text{Ta}_2\text{O}_{5-x}$ /MCN, which holds a spherical morphology with uniform size and clean surface. No undesirable particle aggregation is observed on the

¹Department of Chemical Engineering, Waterloo Institute for Nanotechnology, Waterloo Institute for Sustainable Energy, University of Waterloo, Waterloo, ON N2L 3G1, Canada

²Canadian Light Source, University of Saskatchewan, Saskatoon, Saskatchewan S7N 0X4, Canada

³National-Local Joint Engineering Laboratory for Energy Conservation of Chemical Process, Integration and Resources Utilization, School of Chemical Engineering and Technology, Hebei University of Technology, Tianjin 300130, China

⁴These authors contributed equally

⁵Lead Contact

*Correspondence: zhwchen@uwaterloo.ca
<https://doi.org/10.1016/j.matt.2020.06.002>

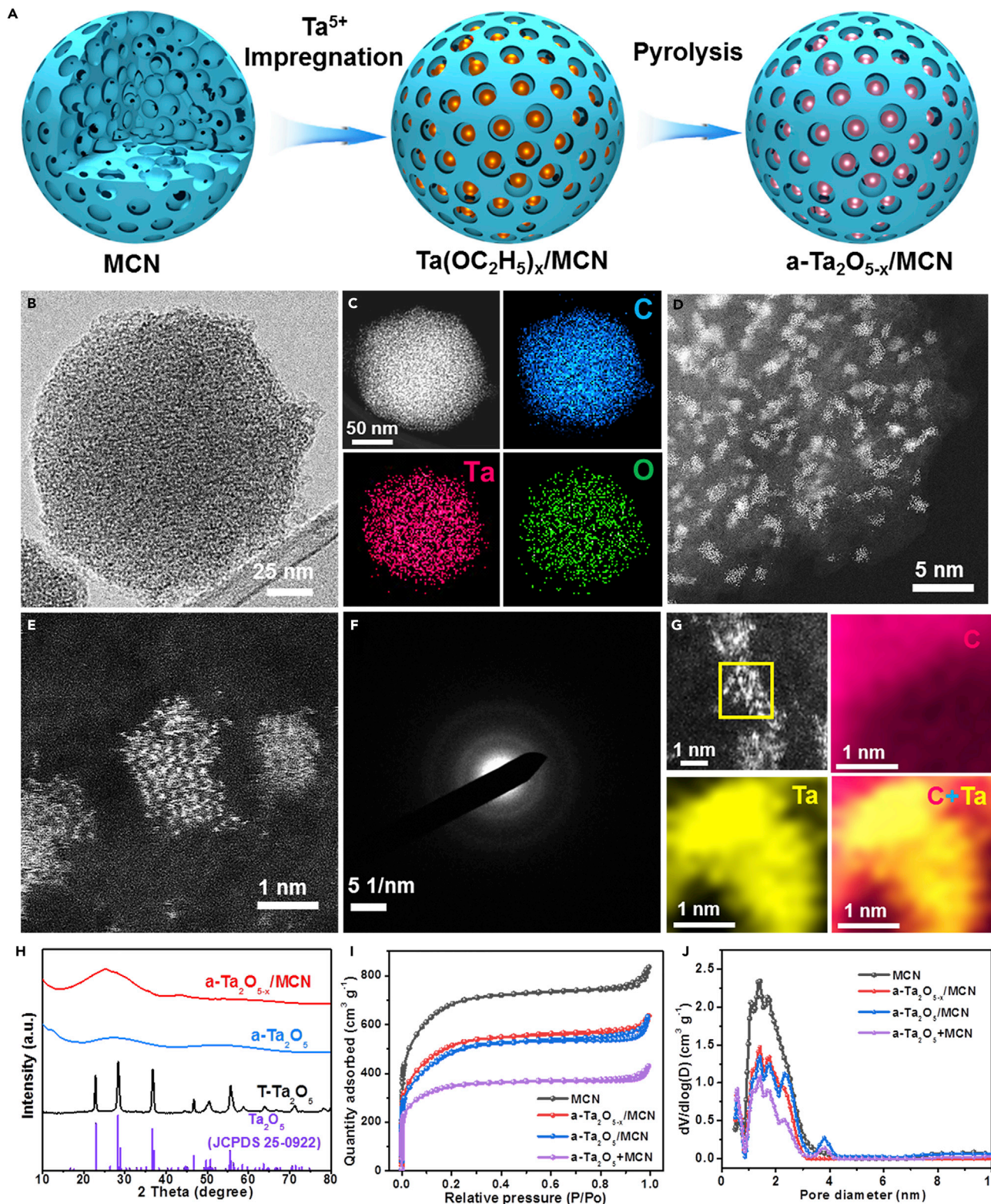


Figure 1. Synthetic Route and Characterizations of Ta-Based Materials

(A) Schematic illustration of the formation of a-Ta₂O_{5-x}/MCN/S.
 (B–F) (B) TEM image, (C) EDS elemental mapping images, (D and E) HAADF-STEM images, and (F) SAED pattern of a-Ta₂O_{5-x}/MCN.
 (G) HAADF-STEM image and corresponding EELS elemental mapping of individual Ta₂O_{5-x} nanocluster accommodated inside carbon pores.
 (H–J) (H) XRD patterns, (I) N₂ adsorption-desorption isotherms, and (J) PSD plots of various samples.

external surface of carbon nanospheres. As displayed in the transmission electron microscopy (TEM) image (Figure 1B), a-Ta₂O_{5-x}/MCN exhibits the same diameter (ca. 150 nm) as MCN without apparent structure change after impregnation of Ta₂O_{5-x}. The energy-dispersive X-ray spectroscopy (EDS) mapping (Figure 1C) manifests the homogeneous distribution of a-Ta₂O_{5-x} throughout the MCN matrix. As demonstrated by the high-angle annular dark-field scanning TEM (HAADF-STEM) image (Figure 1D), the bright Ta₂O_{5-x} nanocluster seeds are uniformly rooted inside the pores of MCN, presenting a pitaya-like structure. The implanted amorphous Ta₂O_{5-x} nanoclusters possess a size of around 1.2 nm (Figure 1E) that is consistent with the nanocluster size distribution (Figure S4). It is worth noting that such tiny nanoclusters could be retained during the high-temperature treatment benefiting from strong spatial confinement effect of carbon pores, which effectively inhibits Ta₂O_{5-x} nanoclusters from agglomeration. The selected area electron diffraction (SAED) pattern (Figure 1F) shows the diffused ring without observable diffraction spots, confirming the amorphous structure of Ta₂O_{5-x} that arises from its confined nucleation by carbon micropores. The HAADF-STEM image in Figure 1G focuses on one individual Ta₂O_{5-x} nanocluster. The corresponding electron energy loss spectroscopy (EELS) mapping demonstrates the intimate contact between built-in Ta₂O_{5-x} nanoclusters and carbon framework, which provides an interconnected conductive network for expediting electron transfer. These results consistently confirm the successful implantation of ultrafine, uniform, and amorphous Ta₂O_{5-x} within the MCN matrix. The mass loading of Ta₂O_{5-x} in the composite is determined to be 23.5 wt % by thermogravimetric analysis (TGA) (Figure S5).

To demonstrate the important role of oxygen vacancies in Ta₂O₅ for Li-S chemistry, we prepared the control sample, a-Ta₂O₅/MCN, by annealing Ta(OC₂H₅)_x/MCN in argon (Ar) atmosphere at the same temperature with a-Ta₂O_{5-x}/MCN. The mass loading of Ta₂O₅ in a-Ta₂O₅/MCN is 23.3 wt % (Figure S6A), which is almost consistent with a-Ta₂O_{5-x}/MCN. To further show the structural merits of a-Ta₂O_{5-x}/MCN as sulfur host, we also prepared three other control samples. First, amorphous Ta₂O₅ (a-Ta₂O₅) was obtained by annealing Ta(OC₂H₅)_x in Ar atmosphere at a low temperature (450°C), as confirmed by X-ray diffraction (XRD) (Figure 1H). a-Ta₂O₅ exhibits a large bulk morphology (Figure S7). The second control sample was obtained by mechanically mixing Ta(OC₂H₅)_x with MCN followed by the same pyrolysis process as a-Ta₂O₅ (denoted as a-Ta₂O₅+MCN). a-Ta₂O₅+MCN has a Ta₂O₅ loading of 23.2 wt % (Figure S6B). Devoid of the pore spatial confinement effect, a-Ta₂O₅+MCN exhibit much larger Ta₂O₅ particles with a microscale size (Figure S8) compared with a-Ta₂O_{5-x}/MCN. Serious aggregation appears in a-Ta₂O₅+MCN, resulting in an uneven distribution of Ta₂O₅ and carbon nanospheres. In addition, the commercial Ta₂O₅ particles with a high crystallinity, as shown in Figure 1H, were applied as another control group (T-Ta₂O₅). The morphology of T-Ta₂O₅ is shown in Figure S9, which exhibits large micrometer-sized particles and severe agglomeration. The amorphous nature of a-Ta₂O_{5-x}/MCN is clearly unveiled by XRD. The two peaks of a-Ta₂O_{5-x}/MCN appearing at 23° and 43° can be indexed to the characteristic (002) and (100) plane of graphitic carbons, respectively.^{22,23} The orthorhombic lattice structure of Ta₂O₅ possesses a long rod-shaped unit cell of 22 Ta atoms and 55 O atoms (lattice parameters: *a* = 6.198 Å, *b* = 40.290 Å, *c* = 3.888 Å).²⁴ Although the pyrolysis temperature of a-Ta₂O_{5-x}/MCN (i.e., 650°C) is enough for the

formation of Ta₂O₅ crystal,²⁴ the carbon micropores with the narrow space confine the nucleation of Ta₂O_{5-x} nanoclusters, which shape an incomplete unit cell in the amorphous structure even at a high temperature.

The pore structures of as-prepared samples were studied by N₂ adsorption-desorption analysis. A characteristic type I isotherm in Figure 1I reveals the microporous nature of MCN,²⁵ which exerts a pore volume of 1.52 cm³ g⁻¹ and specific surface area of 2,501 m² g⁻¹. The narrow pore size distribution (PSD) (Figure 1J) of MCN (ca. 1.3 nm) coincides with the size of Ta₂O_{5-x} nanoclusters implanted inside pores. The desirable pore size is capable of potentially immobilizing Ta₂O_{5-x} nanoclusters to prevent their detachment and restricting their nucleation process to tune crystallinity. After loading of Ta₂O_{5-x} nanoclusters, the a-Ta₂O_{5-x}/MCN inherits well the original microporous structure of MCN, but with a slight reduction in pore volume (1.23 cm³ g⁻¹) and surface area (1,880 m² g⁻¹). Besides, a-Ta₂O₅/MCN also shows a type I isotherm with an adsorption plateau similar to that of a-Ta₂O_{5-x}/MCN. a-Ta₂O₅/MCN possesses a high surface area of 1,846 m² g⁻¹ and pore volume of 1.20 cm³ g⁻¹, both of which are close to those of a-Ta₂O_{5-x}/MCN with 1,880 m² g⁻¹ and 1.23 cm³ g⁻¹, respectively. The consistent shapes of sorption isotherms and PSD curves with the same peak position between MCN, a-Ta₂O_{5-x}/MCN, and a-Ta₂O₅/MCN strongly manifest that Ta₂O₅ nanoclusters root inside the pores. Owing to the strong physical and chemical confinements of the structure, the Ta₂O_{5-x}-loaded micropores can effectively restrain the dissolution of LPS in organic electrolyte. In contrast, a-Ta₂O₅+MCN shows a different PSD plot with weaker peak volume as well as significantly decreased pore volume (0.74 cm³ g⁻¹) and surface area (1,271 m² g⁻¹), implying that the non-uniform mechanical mixing may cause the blockage of pores and thus lower the porosity.

The defect engineering strategy by introducing oxygen vacancies into amorphous Ta₂O_{5-x} aims to improve the intrinsic conductivity and enhance the electrocatalytic activity for sulfur species. In the X-ray photoelectron spectroscopy (XPS) spectra of Ta 4f (Figure 2A), a-Ta₂O₅/MCN exhibits the Ta 4f_{7/2} and 4f_{5/2} peaks at 26.6 and 28.5 eV, respectively, confirming the dominant oxidation state of Ta⁵⁺,²⁶ whereas for a-Ta₂O_{5-x}/MCN, these two peaks shift to lower BE of 26.0 and 27.8 eV, respectively, implying the lower valence state of Ta species arising from the oxygen vacancies. In the O 1s spectra (Figure 2B), three deconvoluted peaks (O1, O2, O4) appear on both a-Ta₂O_{5-x}/MCN and a-Ta₂O₅/MCN. For the strongest O1 peak, it appears at 530.3 eV in a-Ta₂O₅/MCN ascribed to the Ta–O bond²⁷ while there is a positive shift toward a higher BE (530.8 eV) in a-Ta₂O_{5-x}/MCN, strongly evidencing the modified chemical state of Ta–O bond induced by the successful introduction of oxygen vacancies. Besides, the shoulder O2 peak centered at around 531.5 eV indicates the hydroxylated surface, which is conducive to attracting polysulfides;²⁸ the O4 peak appearing at 533.1 eV is associated with the adsorbed moisture.²⁹ It is particularly noteworthy that a-Ta₂O_{5-x}/MCN presents a distinct O3 peak emerging at 532.4 eV, which is attributed to defects with low oxygen coordination.³⁰ This directly suggests the formation of oxygen defects in a-Ta₂O_{5-x}/MCN, which can be further corroborated by electron paramagnetic response (EPR) spectroscopy (Figure 2C). a-Ta₂O_{5-x}/MCN shows a conspicuous signal with a g value of 2.003, signifying the higher oxygen-vacancy concentration in a-Ta₂O_{5-x}/MCN compared with that of a-Ta₂O₅/MCN.³¹ These results all suggest the highly oxygen-deficient nature of a-Ta₂O_{5-x}/MCN.

Further identifications of the electronic structure and local coordination environment were demonstrated by synchrotron-radiation-based X-ray absorption near-edge

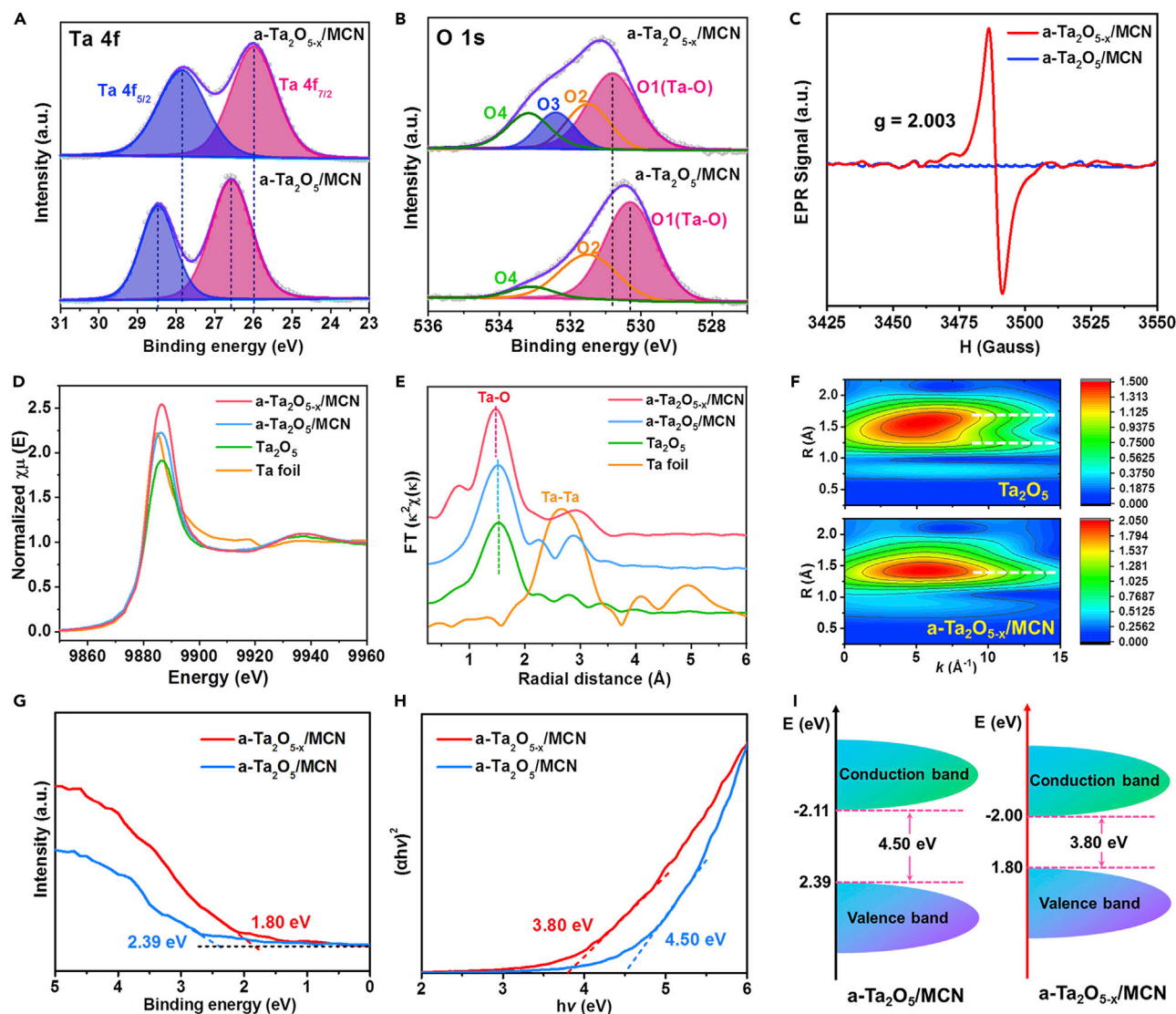


Figure 2. Defect Analysis and Manipulation of Electronic Band Structure

(A–C) High-resolution XPS spectra of (A) Ta 4f and (B) O 1s; (C) EPR patterns for a-Ta₂O_{5-x}/MCN and a-Ta₂O₅/MCN.

(D and E) (D) Ta L₃-edge XANES spectra and (E) FT k³-weighted Ta L₃-edge EXAFS spectra of various samples.

(F) Wavelet transforms for the k³-weighted Ta L₃-edge EXAFS signals of a-Ta₂O_{5-x}/MCN and Ta₂O₅.

(G–I) (G) Valence band XPS spectra, (H) Kubelka-Munk plot, and (I) band diagram of a-Ta₂O_{5-x}/MCN and a-Ta₂O₅/MCN.

structure (XANES) and extended X-ray absorption fine structure (EXAFS) spectroscopy. In the XANES spectra (Figure 2D), the absorption edge of a-Ta₂O_{5-x}/MCN is consistent with Ta₂O₅, indicating the predominant valence state of Ta⁵⁺. The white line at the Ta L₃-edge XANES represents the dipolar transition from 2p core levels to unoccupied Ta 5d states.³² a-Ta₂O_{5-x}/MCN shows the highest white-line intensity, which demonstrates the increased density of Ta 5d unoccupied states near the Fermi level probably induced by the oxygen-vacancy defect.³³ Besides, the Ta L₃ absorption edge energy (E₀) reflects the CBM.³⁴ The E₀ of a-Ta₂O_{5-x}/MCN and a-Ta₂O₅/MCN is 9,882.75 eV and 9,883.82 eV, respectively, which implies that a-Ta₂O_{5-x}/MCN possesses a lower CBM, desirable for electron transition. In the Fourier transformed (FT) k³-weighted EXAFS as shown in Figure 2E, Ta₂O₅ exhibits a single peak with the average bond length of 1.53 Å, corresponding to the Ta–O bond

coordination. For a-Ta₂O₅/MCN, benefiting from the spatial confinement effect, the narrow carbon pore restricts the nucleation and growth of Ta₂O₅, thus resulting in an incomplete unit cell with a short-range ordered structure (i.e., amorphous structure). As such, a reduced Ta–O bond length (1.51 Å) can be found in a-Ta₂O₅/MCN. Besides, the oxygen-deficient environment in a-Ta₂O_{5-x}/MCN further partially disrupts the incomplete amorphous structure, which may impel Ta–O bond coordination to tend toward octahedral TaO₆ (short-range order). As a result, this further shortens the Ta–O bond length (1.47 Å) and enhances the Ta 5d–O 2p orbital overlap with the increased bond covalency around Ta.³⁵ A Cauchy wavelet transform plot (Figure 2F) creates a two-dimensional map of the transform space to highlight the contribution of multiple scattering paths to the EXAFS spectra. The Ta₂O₅ exhibits two scattering paths from $R = 1\text{--}2$ Å in the first coordination shell, which correspond to the Ta–O bond coordination of TaO₆ octahedra and TaO₇ pentagonal bipyramids in the Ta₂O₅ crystal.³⁶ Despite the fact that the obtained a-Ta₂O₅/MCN nanocluster is amorphous and lacks long-range order, it still exhibits the building blocks of TaO₆ and TaO₇ polyhedrons inside the incomplete unit cell. A slightly negative shift of radial distance is observed in a-Ta₂O₅/MCN (Figure S10), corresponding to the bond-length variation attributed to amorphous structure.³⁷ With the introduction of oxygen vacancies into Ta₂O₅, the oxygen-deficient environment weakens partial Ta–O coordination and reduces its radial distance, provoking severe structure distortion,³⁸ and thus there is only one scattering path corresponding to the dominant TaO₆ octahedra present in a-Ta₂O_{5-x}/MCN (Figure 2F).

To elucidate the role of oxygen vacancies in the electrical conductivity, we prepared another control sample, a-Ta₂O_{5-x}, using the same method as for a-Ta₂O₅ except for annealing in H₂ atmosphere to introduce oxygen vacancies. As shown in Figure S11, the oxygen-deficient a-Ta₂O_{5-x} possesses much higher electrical conductivity of 2.1×10^{-2} S m⁻¹ than a-Ta₂O₅ with 4.2×10^{-7} S m⁻¹ and T-Ta₂O₅ with 3.4×10^{-7} S m⁻¹. This demonstrates the crucial role of oxygen vacancies in improving the intrinsic electrical conductivity of Ta₂O₅. In addition, valence band (VB) XPS was performed to investigate the electron band configuration. Figure 2G exhibits the VB XPS spectra and shows the edge of the maximum energy located at 2.39 eV for a-Ta₂O₅/MCN while the VB maximum of a-Ta₂O_{5-x}/MCN moves toward 1.80 eV. Such a blue-shift can be associated with band bending for promoted charge transfer induced by oxygen vacancies.²⁰ The Kubelka-Munk plot (Figure 2H) demonstrates band-gap values of a-Ta₂O₅/MCN and a-Ta₂O_{5-x}/MCN of 4.50 and 3.80 eV, respectively. The narrower band gap of defect-engineered a-Ta₂O_{5-x}/MCN confirms the efficient band engineering. Accordingly, the energy band diagram is illustrated in Figure 2I. a-Ta₂O_{5-x}/MCN presents a lower CBM than a-Ta₂O₅/MCN, which coincides with the XANES results. Besides, the impact from carbon-defect structure was excluded by Raman spectroscopy (Figure S12). Both a-Ta₂O₅/MCN and a-Ta₂O_{5-x}/MCN present similar D/G intensity ratios, indicating their similar degree of carbon defects, which could not contribute to the distinction in band configuration.³⁹ This evidence indicates that oxygen vacancies lead to the formation of new electronic states located in the band gap of Ta₂O₅, which leads to the enhancement of electrical conductivity and fast electron transfer for sulfur electrochemistry.

UV-visible (UV-vis) and XPS measurements were performed to elucidate the LPS adsorption abilities toward enhanced sulfur entrapment. As shown in Figure 3A, the UV-vis spectrum of the pristine Li₂S₆ shows two peaks at 275 and 422 nm, which can be assigned to S₆²⁻ and S₄²⁻, respectively.⁴⁰ a-Ta₂O_{5-x}/MCN exhibits the largest reduction in peak intensity, suggesting its strongest LPS adsorption capabilities. In the XPS spectra of S 2p (Figure 3B), pristine Li₂S₆ demonstrates two sets of

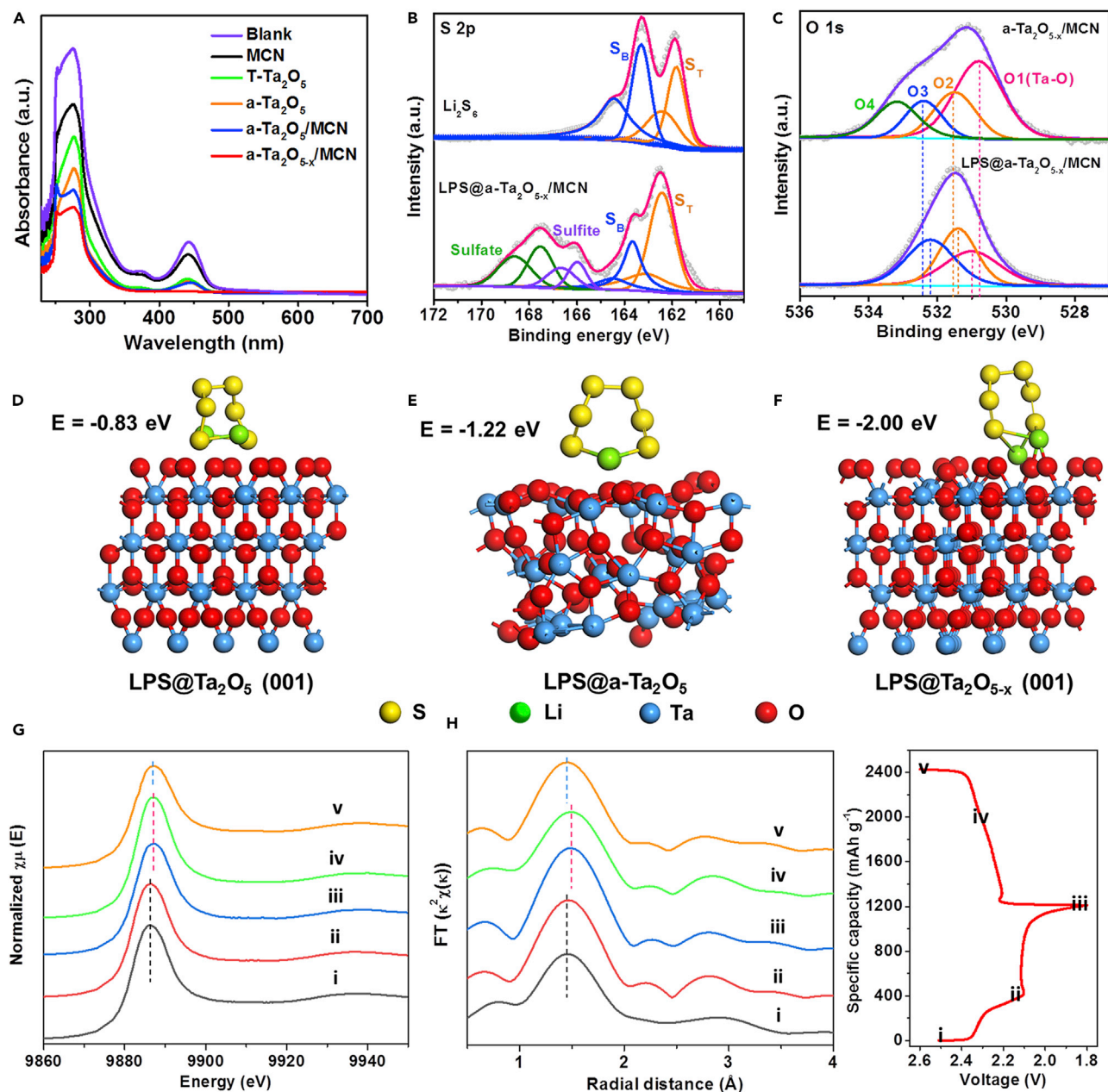


Figure 3. Interactions Between LPS and Ta-Based Materials

(A) UV-vis spectra of LPS solution absorbed by various samples.

(B and C) High-resolution XPS spectra of (B) S 2p for pristine Li_2S_6 and $\text{LPS}@a\text{-Ta}_2\text{O}_{5-x}/\text{MCN}$ and (C) O 1s for $a\text{-Ta}_2\text{O}_{5-x}/\text{MCN}$ and $\text{LPS}@a\text{-Ta}_2\text{O}_{5-x}/\text{MCN}$

(D–F) DFT optimized binding geometric configurations and energies of Li_2S_6 on (D) $\text{LPS}@a\text{-Ta}_2\text{O}_5$ (001), (E) $\text{LPS}@a\text{-Ta}_2\text{O}_5$, and (F) $\text{LPS}@a\text{-Ta}_2\text{O}_{5-x}$ (001).

(G and H) Ex situ (G) Ta $L_{3\text{-edge}}$ XANES spectra and (H) FT k^3 -weighted Ta $L_{3\text{-edge}}$ EXAFS spectra of $a\text{-Ta}_2\text{O}_{5-x}/\text{MCN}/\text{S}$ at different discharge/charge states in first cycle: (i) pristine, discharge to (ii) 2.1 V and (iii) 1.8 V, and charge to (iv) 2.3 V and (v) 2.6 V.

peaks located between 161.8 eV and 163.3 eV, which correspond to the terminal sulfur (S_T) and bridging sulfur (S_B) of LPS, respectively.⁴¹ After interacting with $a\text{-Ta}_2\text{O}_{5-x}/\text{MCN}$, a large positive shift can be observed in $\text{LPS}@a\text{-Ta}_2\text{O}_{5-x}/\text{MCN}$, confirming the strong chemical interactions between $a\text{-Ta}_2\text{O}_{5-x}/\text{MCN}$ and LPS. Two pairs of broad peaks emerging at the high BE region can be assigned to the formation of sulfite and sulfate on the surface, which offers strong chemical interaction

with LPS.⁴² Besides, the O1 peak of LPS@a-Ta₂O_{5-x}/MCN in Figure 3C shifts toward higher BE corresponding to the reduced electron cloud density of oxygen, demonstrating the “lithium bond”-like interaction.⁴³ The O2 and O3 peaks shift toward lower BE, revealing the coordination between sulfur and oxygen vacancies, corresponding to LPS adsorption on defects.⁴⁴ The enhanced LPS adsorption of amorphous and defective structure were examined by density functional theory (DFT) calculations based on the VASP (Vienna *ab initio* Simulation Package) (Figures 3D–3F). The configuration optimization of a-Ta₂O₅ was based on the T-Ta₂O₅ configuration where all atoms were allowed to relax. T-Ta₂O₅ and a-Ta₂O₅ employed the same cleaved surface for comparing their surface adsorbability. The crystalline T-Ta₂O₅ (001) shows a relatively low Li₂S₆ adsorption energy (E_{ads}) of -0.83 eV with a Li–O bond length of 2.52 Å, corresponding to its limited chemical confinement of LPS. Meanwhile, a-Ta₂O₅ exhibits a stronger E_{ads} of -1.22 eV and shorter Li–O bond length of 2.25 Å, suggesting enhanced LPS adsorption capability of amorphous structure. The higher adsorption energy of amorphous structure could be attributed to the polar surface rearrangement, which strengthens the chemical affinity to LPS. Moreover, the defective structure greatly improves the Li₂S₆ BE by offering a higher E_{ads} (-2.0 eV) and significantly strengthened Li–O bond (1.86 Å), revealing the excellent LPS confinement on oxygen defects of Ta₂O_{5-x}. The higher E_{ads} of amorphous and defective structure ensures a highly reversible LPS adsorption-conversion-desorption process, which could be utilized as an electrocatalyst to accelerate LPS conversion kinetics in Li-S batteries.⁴⁵

The corresponding sulfur electrodes of various samples were developed via a melt-impregnation method. The TGA (Figure S13) indicates a sulfur content of 66.2 wt % in the sulfur composite. As shown in Figure S14, there is no apparent structure change or particle agglomeration after impregnation of sulfur, which was confined within pores of a-Ta₂O_{5-x}/MCN. The EDS mapping (Figure S15) demonstrates a homogeneous distribution of S throughout a-Ta₂O_{5-x}/MCN/S matrix. As revealed by XRD (Figure S16), a-Ta₂O_{5-x}/MCN/S still exhibits an amorphous structure, and no crystalline S peaks are observed. The characteristic *Fddd* orthorhombic crystal structure peaks of element S disappear from the XRD pattern of a-Ta₂O_{5-x}/MCN/S, which indicates that embedded S existed in ultrafine particles and a highly dispersed amorphous state. This is due to the spatial confinement of nanosized S inside the micropores, which could have prohibited the crystallization of nanosulfur.⁴⁶ In the Raman spectra (Figure S17), the characteristic S-S band of the a-Ta₂O_{5-x}/MCN/S is not detected, which coincides with the XRD results. This evidence confirms that S was strongly confined within the micropores of a-Ta₂O_{5-x}/MCN/S in a homogeneous distribution and was hardly exposed to the external surface by virtue of the pitaya-like architecture.

The *ex situ* Ta *L*₃-edge XANES and EXAFS of a-Ta₂O_{5-x}/MCN/S at different applied potentials in the first cycle were used to determine the valence and chemical environment change during the charge-discharge process. In XANES spectra (Figure 3G), a-Ta₂O_{5-x}/MCN/S shows the white-line peaks of 9,886.3 eV at status i and ii, which positively shift to 9,887 eV at status iii and iv and shifts back to 9,886.8 eV at status v, indicating the reversible Ta valence change during the lithiation-delithiation process. Correspondingly, the FT *k*³-weighted EXAFS spectra (Figure 3H) reveal a short radial distance of 1.47 Å at status i and ii and enlargement to 1.53 Å at status iii and iv, confirming strong chemical interaction between LPS and a-Ta₂O_{5-x}/MCN. Moreover, the radial distance switches back to 1.43 Å after charging to 2.6 V (status v). The reversible bond-length variation suggests the reversibility of structure change during the charge-discharge process, revealing the stability of oxygen-deficient structure.

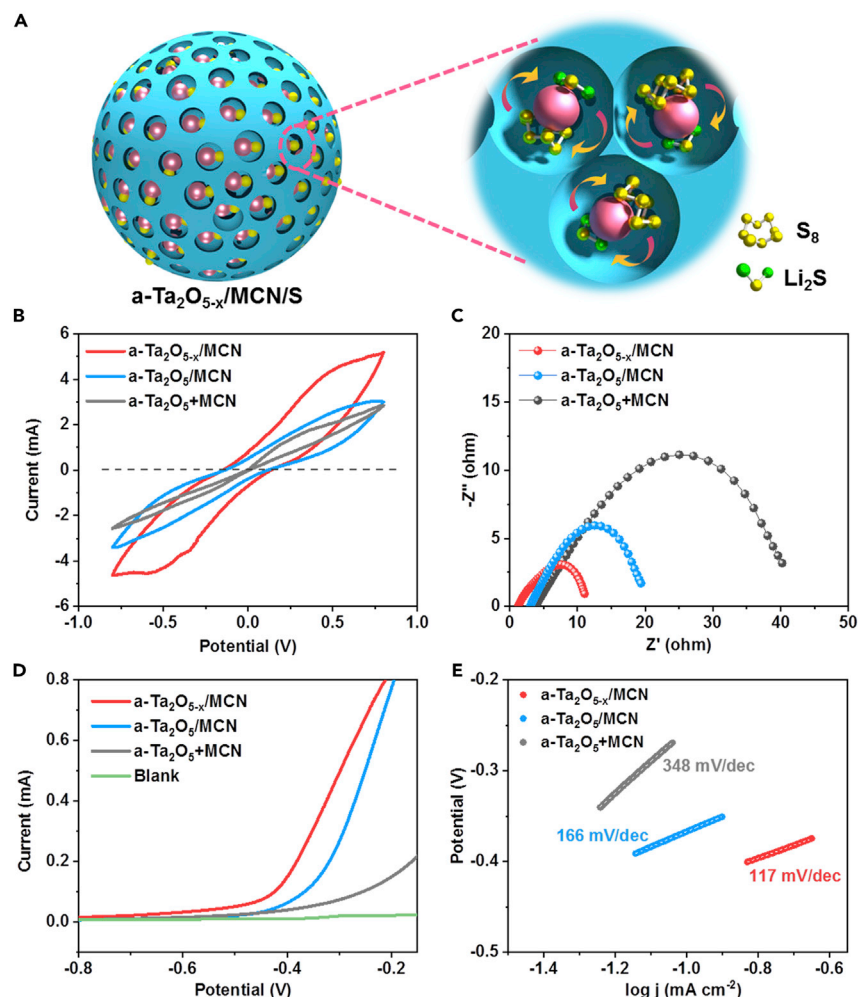


Figure 4. Electrochemical Analysis of Ta-Based Materials

(A) Scheme illustration of LPS catalytic conversion in nanoreactor.

(B–E) (B) CV curves, (C) EIS spectra of Li_2S_6 symmetrical cells, (D) LSV curves, and (E) Tafel plots of Li_2S oxidation on a- $\text{Ta}_2\text{O}_{5-x}/\text{MCN}$, a- $\text{Ta}_2\text{O}_5/\text{MCN}$, and a- $\text{Ta}_2\text{O}_5+\text{MCN}$.

The above evidence implies that a- $\text{Ta}_2\text{O}_{5-x}/\text{MCN}$ could function as a promising electrocatalyst for sulfur redox reactions. The nanopores loaded with amorphous $\text{Ta}_2\text{O}_{5-x}$ nanoclusters function as a 3D nanoreactor for fast and durable LPS catalytic conversion (Figure 4A). Symmetrical cells were assembled using a- $\text{Ta}_2\text{O}_{5-x}/\text{MCN}$, a- $\text{Ta}_2\text{O}_5/\text{MCN}$, and a- $\text{Ta}_2\text{O}_5+\text{MCN}$ identical electrodes and a Li_2S_6 electrolyte to investigate the LPS conversion kinetics. As displayed in Figure 4B, a- $\text{Ta}_2\text{O}_{5-x}/\text{MCN}$ presents strong redox peaks with the highest current response among different samples, suggesting its faster and more efficient LPS conversions. Besides, electrochemical impedance spectroscopy (EIS) spectra show the lowest electrochemical resistance for a- $\text{Ta}_2\text{O}_{5-x}/\text{MCN}$ (Figure 4C), further confirming its fast charge transfer and facile sulfur redox reactions. In addition, three-electrode linear sweep voltammetry (LSV) measurements were conducted to specifically investigate the Li_2S oxidation behavior (Figure 4D). a- $\text{Ta}_2\text{O}_{5-x}/\text{MCN}$ delivers the highest current response and the lowest onset potential of -0.56 V in comparison with a- $\text{Ta}_2\text{O}_5/\text{MCN}$ (-0.45 V) and a- $\text{Ta}_2\text{O}_5+\text{MCN}$ (-0.4 V), implying the lowest energy barrier for Li_2S oxidation conversion and revealing the superior catalytic activity of

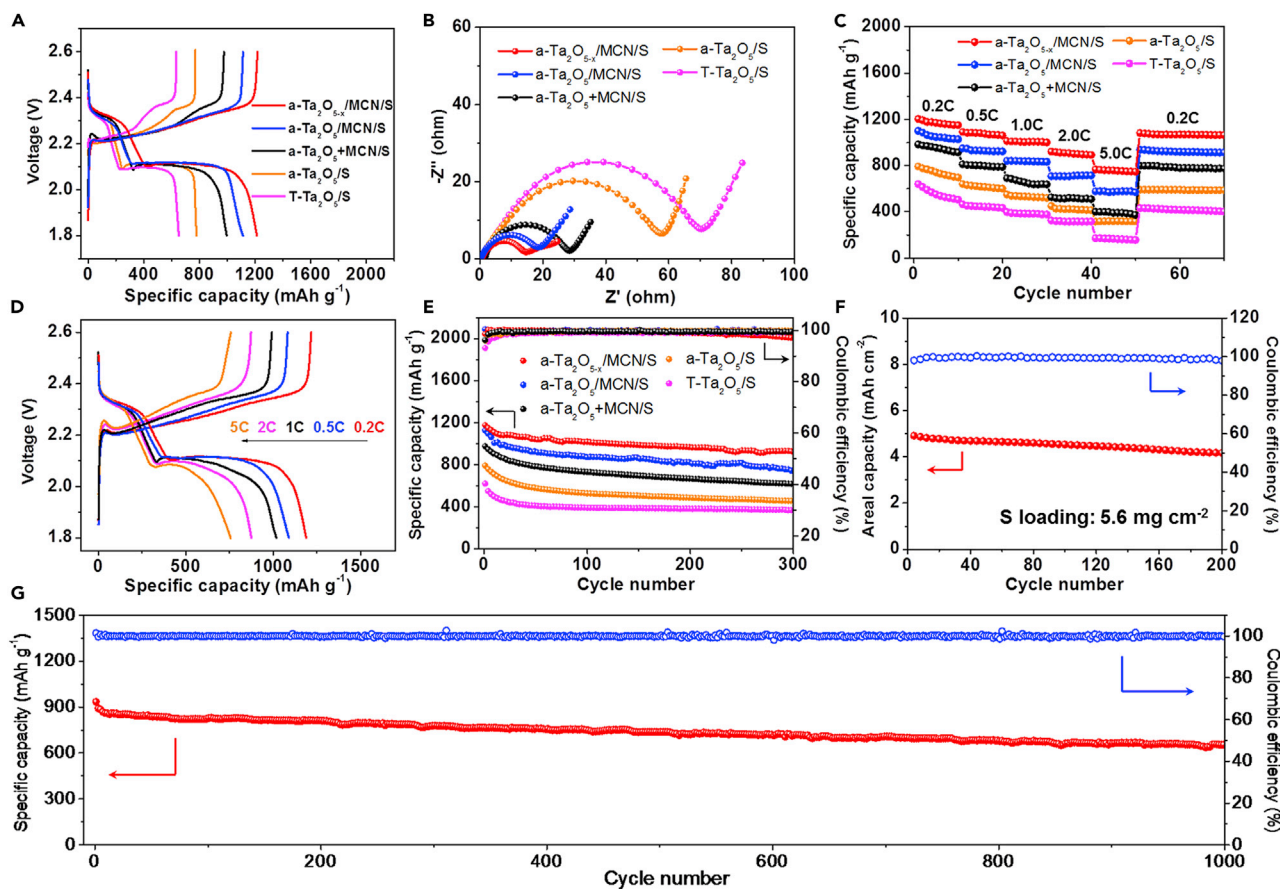


Figure 5. Electrochemical Performances of Ta-Based Sulfur Electrodes

(A) Charge-discharge profiles at 0.2 C, (B) Nyquist plots, (C) rate performance, and (E) cycle performances at 0.2 C of various sulfur electrodes. (D) Multi-rate discharge-charge profiles, (F) areal capacities and cycle performances with high sulfur loading of 5.6 mg cm⁻² and low E/S ratio of 3.6 mL g⁻¹ at 0.2 C, and (G) long cycling performances at 1 C of a-Ta₂O_{5-x}/MCN/S electrode.

a-Ta₂O_{5-x}/MCN. This result can be further supported by the Tafel plot (Figure 4E), which shows a much smaller Tafel slope of 117 mV dec⁻¹ for a-Ta₂O_{5-x}/MCN compared with those for a-Ta₂O₅/MCN (166 mV dec⁻¹) and a-Ta₂O₅+MCN (348 mV dec⁻¹), confirming the remarkable kinetic enhancement owing to the defect-rich and Ta₂O_{5-x}-loaded nanoreactor design. All these results strongly reveal the superior catalytic activity of the a-Ta₂O_{5-x}/MCN toward expedited LPS conversion.

Electrochemical evaluations were performed to demonstrate the enhanced Li-S performances for a-Ta₂O_{5-x}/MCN/S. The charge-discharge profiles of sulfur composites display two plateau curves (Figure 5A). The discharge plateaus at 2.3 and 2.1 V (versus Li⁺/Li) are associated with the electroreduction of sulfur into long-chain LPS and further reduction to Li₂S₂/Li₂S, corresponding to the cyclic voltammetry (CV) results that show two major reduction peaks and two oxidation peaks (Figure S18). Compared with T-Ta₂O₅/S, the a-Ta₂O₅/S electrode displays higher discharge capacity and smaller polarization, suggesting the contribution of amorphous structure to improved Li-S performance. Moreover, a-Ta₂O_{5-x}/MCN/S exhibits the lowest potential hysteresis in charge-discharge profiles and CV curve, with enhanced discharge capacity (around 1,200 mAh g⁻¹) and current response, respectively. The defect-rich amorphous Ta₂O₅ implanted within the interconnected micropores of MCN strengthens its ionic/electronic

conductivity, which acts as the nanoreactor to accelerate LPS redox reaction, leading to fast and durable electrochemical performance. Figure 5B exhibits the Nyquist plots of various sulfur electrodes, where the semicircle at the medium-frequency region corresponds to the charge-transfer impedance, and the slope at the low-frequency region corresponds to Warburg impedance for diffusion process.⁴⁷ a-Ta₂O_{5-x}/MCN/S presents the smallest charge-transfer and Warburg resistance, indicating its best charge and mass transfer features. The rate performances and corresponding charge-discharge profiles are displayed in Figures 5C, 5D, and S19. a-Ta₂O_{5-x}/MCN/S delivers the best rate performance with the highest discharge capacity of 766 mAh g⁻¹ at 5 C compared with a-Ta₂O₅/MCN/S (600 mAh g⁻¹) and a-Ta₂O₅+MCN/S (380 mAh g⁻¹), and the reversible capacity of 1,080.9 mAh g⁻¹ when the current returns to 0.2 C. These results congruously confirm that the enhanced catalytic activity and kinetics for LPS conversion are due to the elaborate design of a-Ta₂O_{5-x}/MCN/S composite. The cycling performances are compared at a current density of 0.2 C (Figure 5E). a-Ta₂O_{5-x}/MCN/S presents the best cyclability with a high discharge capacity of 913.7 mAh g⁻¹ and high Coulombic efficiency after 300 cycles. In the long-term cycling testing, a-Ta₂O₅/MCN/S electrode exerts a durable cycling performance over 600 cycles at 1 C (Figure S20). After introducing oxygen vacancies, a-Ta₂O_{5-x}/MCN/S exhibits superior cyclic stability over 1,000 cycles with a remarkably low capacity fading rate of 0.029% per cycle (Figure 5G). As shown in Figure S21, a-Ta₂O_{5-x}/MCN/S still exhibits a decent capacity of 680 mAh g⁻¹ after 1,000 cycles. This performance is very competitive compared with other reported electrodes based on transition metal/porous carbon composites (Table S1). a-Ta₂O_{5-x}/MCN with a pitaya-like nanoreactor guarantees sulfur homogenization and facilitated ion/electron conduction, and offers strong chemical and physical confinements to suppress an LPS shuttle effect. The successful introduction of oxygen vacancies further improves electronic conduction within the electrode and provides electrocatalytic sites promoting the chemical interaction with LPS and sulfur redox kinetics.

High sulfur loading and low electrolyte/sulfur (E/S) ratio are critical for achieving high areal capacity and energy density toward Li-S battery practicalization. The charge-discharge profile of a-Ta₂O_{5-x}/MCN/S electrode for high-sulfur-loading performance (Figure S22) delivers a high areal capacity (5 mAh cm⁻²) under high sulfur loading (5.6 mg cm⁻²) and low E/S ratio (3.6 mL g⁻¹). a-Ta₂O_{5-x}/MCN/S exhibits an excellent cyclability with high areal capacity over 4 mAh cm⁻² after 200 cycles (Figure 5F). The rate performance of a-Ta₂O_{5-x}/MCN/S was also investigated at the practically relevant condition. As shown in Figure S23, a-Ta₂O_{5-x}/MCN/S delivers a decent capacity over 2.5 mAh cm⁻² under a high current density of 2 C and reversible capacity of 4.7 mAh cm⁻² when the current returns to 0.2 C. The excellent cyclability and rate capability of a-Ta₂O_{5-x}/MCN/S benefit from its potent shuttling inhibition and superior electrocatalytic activity and kinetics for fast LPS conversion to facilitate sulfur utilization. These results reveal high promise in the practical application of Li-S batteries.

Conclusions

Taking advantage of the electronic properties specific to tantalum, we developed amorphous tantalum oxide with oxygen vacancies implanted inside a microporous carbon matrix as a new electrocatalyst toward polysulfide catalysis and retention. Carbon nanopores restrict the nucleation of Ta₂O_{5-x} nanoseeds to shape the incomplete unit cell in an amorphous structure with enlarged active surfaces, which reduces the Ta–O bond length and provides strong chemical affinity for LPS. The oxygen vacancies further tune the Ta–O local coordination environment and electron band structure of Ta₂O_{5-x} to improve the intrinsic electrical conductivity and function as catalytic centers. The engineered 3D conductive nanoreactor loaded with

Ta₂O_{5-x} nanoclusters efficiently inhibits LPS shuttling and promotes LPS catalyzation with fast redox kinetics. Meanwhile, the sulfur agglomeration and volume expansion are well suppressed in the pitaya-like structure. These featuring superiorities endow the developed sulfur electrode with outstanding rate capability and cyclability even at practically relevant sulfur loading and electrolyte content. We believe that our identification of tantalum as a new catalyst material for Li-S batteries will stimulate more efforts on the specific selection of transition metals based on their electronic structures. The unique “ship in a bottle” strategy offers guidance for rational structural design in energy conversion and storage systems.

EXPERIMENTAL PROCEDURES

Resource Availability

Lead Contact

Further information and requests for resources and reagents should be directed to and will be fulfilled by the Lead Contact, Prof. Zhongwei Chen (zhwchen@uwaterloo.ca).

Materials Availability

This study did not generate new unique reagents. All materials used in this work are commercially available.

Data and Code Availability

All the necessary data supporting the main findings of the paper are available within the main paper and its [Supplemental Information](#) files and from the Lead Contact upon reasonable request.

Preparation of MCN

In a typical synthesis, a 70-mL aqueous solution of 0.7 M glucose was sealed in a Teflon-lined stainless-steel autoclave and hydrothermally treated at 185°C for 6 h. The collected precipitate was washed several times with deionized water. After drying at 80°C for 12 h, small amount of ZnCl₂ aqueous solution was added to the carbonaceous powder at a 5:1 weight ratio of ZnCl₂ to powder under stirring for 6 h. The suspension was dried in an oven at 110°C to vaporize the visible water, after which the collected solid was vacuum dried for 20 h. Following this, the powder underwent pyrolysis at 850°C for 2 h in the carbon dioxide atmosphere. The obtained samples were immersed in dilute hydrochloric acid under stirring and then washed with deionized water, resulting in the formation of MCN.

Preparation of a-Ta₂O_{5-x}/MCN and a-Ta₂O₅/MCN

Typically, tantalum(V) chloride was added into the anhydrous ethanol under ultrasonication for 2 h. A small amount of the prepared solution was then added to MCN in a well-dried glass vial, which was quickly capped and underwent ultrasonication for 3 h. After drying at 85°C in vacuum for 12 h, the powder was transferred to the tube furnace and pyrolyzed in the hydrogen atmosphere at the flow rate of 80 sccm at 650°C for 2 h to yield a-Ta₂O_{5-x}/MCN. The control sample, a-Ta₂O₅/MCN, was synthesized using the above method except for annealing in Ar atmosphere.

Preparation of a-Ta₂O₅ and a-Ta₂O_{5-x}

The prepared tantalum(V) chloride ethanol solution was directly dried at 80°C under vacuum overnight. The collected solid was then heated in Ar atmosphere at 450°C for 1 h to obtain the amorphous Ta₂O₅ (a-Ta₂O₅).⁴⁸ The control sample, a-Ta₂O_{5-x}, was prepared by the same method as a-Ta₂O₅ except for annealing in the H₂ atmosphere.

Preparation of a-Ta₂O₅+MCN

The prepared tantalum(V) chloride ethanol solution was directly dried at 80°C in vacuum for 12 h. Next, the obtained powder was mechanically mixed with MCN with the same Ta₂O₅ content as a-Ta₂O_{5-x}/MCN and a-Ta₂O₅/MCN. The as-prepared sample was heated in Ar atmosphere at 450°C for 1 h to yield a-Ta₂O₅+MCN.

The details of materials characterization, electrochemical measurements, and DFT calculations are provided in [Supplemental Experimental Procedures](#).

SUPPLEMENTAL INFORMATION

Supplemental Information can be found online at <https://doi.org/10.1016/j.matt.2020.06.002>.

ACKNOWLEDGMENTS

We appreciate the support from the Natural Sciences and Engineering Research Council of Canada, University of Waterloo, Dr. David Muir in Canadian Light Source with the XAS characterizations, Dr. Dong Su from Brookhaven National Laboratory, and Dr. Carmen Andrei from the Canadian Center for Electron Microscopy at McMaster University for electron microscopy characterizations.

AUTHOR CONTRIBUTIONS

Conceptualization, Z.C., Z.Z., and D.L.; Methodology, Z.Z. and D.L.; Formal Analysis, Z.Z., D.L., R.G., and J.L.; Investigation, Z.Z., D.L., S.L., L.Z., H.D., and G.W.; Resources, Z.C., A.Y., and Y.H.; Writing – Original Draft, Z.Z. and D.L.; Writing – Review & Editing, Z.C., Z.Z., D.L., G.L., and M.L.; Visualization, Z.Z. and S.S.; Supervision, Z.C. and A.Y.; Project Administration, Z.C.; Funding Acquisition, Z.C. and A.Y.

DECLARATION OF INTERESTS

The authors declare no competing interests.

Received: March 2, 2020

Revised: May 7, 2020

Accepted: May 29, 2020

Published: June 30, 2020

REFERENCES

1. Cao, Y., Li, M., Lu, J., Liu, J., and Amine, K. (2019). Bridging the academic and industrial metrics for next-generation practical batteries. *Nat. Nanotechnol.* *14*, 200–207.
2. Cano, Z.P., Banham, D., Ye, S., Hintennach, A., Lu, J., Fowler, M., and Chen, Z. (2018). Batteries and fuel cells for emerging electric vehicle markets. *Nat. Energy* *3*, 279–289.
3. Xie, J., Peng, H.-J., Huang, J.-Q., Xu, W.-T., Chen, X., and Zhang, Q. (2017). A supramolecular capsule for reversible polysulfide storage/delivery in lithium-sulfur batteries. *Angew. Chem. Int. Ed.* *56*, 16223–16227.
4. Wu, F., Chen, S., Srot, V., Huang, Y., Sinha, S.K., van Aken, P.A., Maier, J., and Yu, Y. (2018). A sulfur-limonene-based electrode for lithium-sulfur batteries: high-performance by self-protection. *Adv. Mater.* *30*, 1706643.
5. Son, Y., Lee, J.-S., Son, Y., Jang, J.-H., and Cho, J. (2015). Recent advances in lithium sulfide cathode materials and their use in lithium sulfur batteries. *Adv. Energy Mater.* *5*, 1500110.
6. Wu, X., Markir, A., Xu, Y., Hu, E.C., Dai, K.T., Zhang, C., Shin, W., Leonard, D.P., Kim, K., and Ji, X. (2019). Rechargeable iron-sulfur battery without polysulfide shuttling. *Adv. Energy Mater.* *9*, 1902422.
7. Wang, X., Li, G., Li, J., Zhang, Y., Wook, A., Yu, A., and Chen, Z. (2016). Structural and chemical synergistic encapsulation of polysulfides enables ultralong-life lithium-sulfur batteries. *Energy Environ. Sci.* *9*, 2533–2538.
8. Zhou, T., Lv, W., Li, J., Zhou, G., Zhao, Y., Fan, S., Liu, B., Li, B., Kang, F., and Yang, Q.-H. (2017). Twinborn TiO₂-TiN heterostructures enabling smooth trapping-diffusion-conversion of polysulfides towards ultralong life lithium-sulfur batteries. *Energy Environ. Sci.* *10*, 1694–1703.
9. Xue, W., Yu, D., Suo, L., Wang, C., Wang, Z., Xu, G., Xiao, X., Ge, M., Ko, M., Chen, Y., et al. (2019). Manipulating sulfur mobility enables advanced Li-S batteries. *Matter* *1*, 1047–1060.
10. Song, Y., Sun, Z., Cai, J., Wei, N., Wang, M., Shao, Y., Liu, Z., and Sun, J. (2019). Accelerated Li-S chemistry at a cooperative interface built in situ. *J. Mater. Chem. A* *7*, 20750–20759.
11. Wang, S., Liao, J., Yang, X., Liang, J., Sun, Q., Liang, J., Zhao, F., Koo, A., Kong, F., Yao, Y., et al. (2019). Designing a highly efficient polysulfide conversion catalyst with paramontroseite for high-performance and long-life lithium-sulfur batteries. *Nano Energy* *57*, 230–240.
12. Lin, H., Yang, L., Jiang, X., Li, G., Zhang, T., Yao, Q., Zheng, G.W., and Lee, J.Y. (2017). Electrocatalysis of polysulfide conversion by

- sulfur-deficient MoS₂ nanoflakes for lithium-sulfur batteries. *Energy Environ. Sci.* **10**, 1476–1486.
13. Liu, Y., Han, M., Xiong, Q., Zhang, S., Zhao, C., Gong, W., Wang, G., Zhang, H., and Zhao, H. (2019). Dramatically enhanced ambient ammonia electrosynthesis performance by in-operando created Li-S interactions on MoS₂ electrocatalyst. *Adv. Energy Mater.* **9**, 1803935.
 14. Chhowalla, M., Shin, H.S., Eda, G., Li, L.-J., Loh, K.P., and Zhang, H. (2013). The chemistry of two-dimensional layered transition metal dichalcogenide nanosheets. *Nat. Chem.* **5**, 263–275.
 15. He, J., and Manthiram, A. (2019). A review on the status and challenges of electrocatalysts in lithium-sulfur batteries. *Energy Storage Mater.* **20**, 55–70.
 16. Zhang, C., Lv, W., Zhang, W., Zheng, X., Wu, M.-B., Wei, W., Tao, Y., Li, Z., and Yang, Q.-H. (2014). Reduction of graphene oxide by hydrogen sulfide: a promising strategy for pollutant control and as an electrode for Li-S batteries. *Adv. Energy Mater.* **4**, 1301565.
 17. Chen, D., Qiao, M., Lu, Y.-R., Hao, L., Liu, D., Dong, C.-L., Li, Y., and Wang, S. (2018). Preferential cation vacancies in perovskite hydroxide for the oxygen evolution reaction. *Angew. Chem. Int. Ed.* **57**, 8691–8696.
 18. Zhang, P., Zhang, J., and Gong, J. (2014). Tantalum-based semiconductors for solar water splitting. *Chem. Soc. Rev.* **43**, 4395–4422.
 19. Chun, W.-J., Ishikawa, A., Fujisawa, H., Takata, T., Kondo, J.N., Hara, M., Kawai, M., Matsumoto, Y., and Domen, K. (2003). Conduction and valence band positions of Ta₂O₅, TaON, and Ta₃N₅ by UPS and electrochemical methods. *J. Phys. Chem. B* **107**, 1798–1803.
 20. Wang, Y., Zhang, R., Chen, J., Wu, H., Lu, S., Wang, K., Li, H., Harris, C.J., Xi, K., Kumar, R.V., et al. (2019). Enhancing catalytic activity of titanium oxide in lithium-sulfur batteries by band engineering. *Adv. Energy Mater.* **9**, 1900953.
 21. Mal'chik, A.G., Kuznetsova, S.A., Kryuchkova, S.O., and Kozik, V.V. (2017). Sol-gel synthesis of Ta₂O₅-SiO₂ composites from tantalum(V) chloride and tetraethyl orthosilicate in ethanol. *Inorg. Mater.* **53**, 994–1003.
 22. Etacheri, V., Wang, C., O'Connell, M.J., Chan, C.K., and Pol, V.G. (2015). Porous carbon sphere anodes for enhanced lithium-ion storage. *J. Mater. Chem. A* **3**, 9861–9868.
 23. Zhang, Z., Cano, Z.P., Luo, D., Dou, H., Yu, A., and Chen, Z. (2019). Rational design of tailored porous carbon-based materials for CO₂ capture. *J. Mater. Chem. A* **7**, 20985–21003.
 24. Joseph, C., Bourson, P., and Fontana, M.D. (2012). Amorphous to crystalline transformation in Ta₂O₅ studied by Raman spectroscopy. *J. Raman Spectrosc.* **43**, 1146–1150.
 25. Zhang, Z., Luo, D., Lui, G., Li, G., Jiang, G., Cano, Z.P., Deng, Y.-P., Du, X., Yin, S., Chen, Y., et al. (2019). In-situ ion-activated carbon nanospheres with tunable ultramicroporosity for superior CO₂ capture. *Carbon* **143**, 531–541.
 26. Xia, S., Ni, J., Savilov, S.V., and Li, L. (2018). Oxygen-deficient Ta₂O₅ nanoporous films as self-supported electrodes for lithium microbatteries. *Nano Energy* **45**, 407–412.
 27. Carneiro, J.F., Rocha, R.S., Hammer, P., Bertazzoli, R., and Lanza, M.R.V. (2016). Hydrogen peroxide electrogeneration in gas diffusion electrode nanostructured with Ta₂O₅. *Appl. Catal. Gen.* **517**, 161–167.
 28. Yuan, C., Li, J., Hou, L., Zhang, X., Shen, L., and Lou (David), X.W. (2012). Ultrathin mesoporous NiCo₂O₄ nanosheets supported on Ni foam as advanced electrodes for supercapacitors. *Adv. Funct. Mater.* **22**, 4592–4597.
 29. Luo, D., Li, G., Deng, Y.-P., Zhang, Z., Li, J., Liang, R., Li, M., Jiang, Y., Zhang, W., Liu, Y., et al. (2019). Synergistic engineering of defects and architecture in binary metal chalcogenide toward fast and reliable lithium-sulfur batteries. *Adv. Energy Mater.* **9**, 1900228.
 30. Gao, R., Li, Z., Zhang, X., Zhang, J., Hu, Z., and Liu, X. (2016). Carbon-dotted defective CoO with oxygen vacancies: a synergetic design of bifunctional cathode catalyst for Li-O₂ batteries. *ACS Catal.* **6**, 400–406.
 31. Zhang, Y., Mu, Z., Yang, C., Xu, Z., Zhang, S., Zhang, X., Li, Y., Lai, J., Sun, Z., Yang, Y., et al. (2018). Rational design of MXene/1T-2H MoS₂-C nanohybrids for high-performance lithium-sulfur batteries. *Adv. Funct. Mater.* **28**, 1707578.
 32. Brown, M., Peierls, R.E., and Stern, E.A. (1977). White lines in x-ray absorption. *Phys. Rev. B* **15**, 738–744.
 33. Tsuchiya, T., Imai, H., Miyoshi, S., Glans, P.-A., Guo, J., and Yamaguchi, S. (2011). X-Ray absorption, photoemission spectroscopy, and Raman scattering analysis of amorphous tantalum oxide with a large extent of oxygen nonstoichiometry. *Phys. Chem. Chem. Phys.* **13**, 17013.
 34. Gatewood, D.S., Schull, T.L., Baturina, O., Pietron, J.J., Garsany, Y., Swider-Lyons, K.E., and Ramaker, D.E. (2008). Characterization of ligand effects on water activation in triarylphosphine-stabilized Pt nanoparticle catalysts by X-ray absorption spectroscopy. *J. Phys. Chem. C* **112**, 4961–4970.
 35. Paek, S.-M., and Kim, Y.-I. (2014). Ta L₃-edge XANES study of perovskite oxynitrides ATaO₂N (A=Ca, Sr, Ba). *J. Alloys Compd.* **587**, 251–254.
 36. Ramprasad, R. (2003). First principles study of oxygen vacancy defects in tantalum pentoxide. *J. Appl. Phys.* **94**, 5609–5612.
 37. Pickup, D.M., Mountjoy, G., Holland, M.A., Wallidge, G.W., Newport, R.J., and Smith, M.E. (2000). Structure of (Ta₂O₅)_x(SiO₂)_{1-x} xerogels (x = 0.05, 0.11, 0.18, 0.25 and 1.0) from FTIR, ²⁹Si and ¹⁷O MAS NMR and EXAFS. *J. Mater. Chem.* **10**, 1887–1894.
 38. Denny, Y.R., Firmansyah, T., Oh, S.K., Kang, H.J., Yang, D.-S., Heo, S., Chung, J., and Lee, J.C. (2016). Effect of oxygen deficiency on electronic properties and local structure of amorphous tantalum oxide thin films. *Mater. Res. Bull.* **82**, 1–6.
 39. Zhang, Z., Deng, Y.-P., Xing, Z., Luo, D., Sy, S., Cano, Z.P., Liu, G., Jiang, Y., and Chen, Z. (2019). "Ship in a bottle" design of highly efficient bifunctional electrocatalysts for long-lasting rechargeable Zn-air batteries. *ACS Nano* **13**, 7062–7072.
 40. Cai, W., Li, G., Zhang, K., Xiao, G., Wang, C., Ye, K., Chen, Z., Zhu, Y., and Qian, Y. (2018). Conductive nanocrystalline niobium carbide as high-efficiency polysulfides tamer for lithium-sulfur batteries. *Adv. Funct. Mater.* **28**, 1704865.
 41. Wang, J., Liang, J., Wu, J., Xuan, C., Wu, Z., Guo, X., Lai, C., Zhu, Y., and Wang, D. (2018). Coordination effect of network NiO nanosheet and a carbon layer on the cathode side in constructing a high-performance lithium-sulfur battery. *J. Mater. Chem. A* **6**, 6503–6509.
 42. Li, G., Lei, W., Luo, D., Deng, Y., Deng, Z., Wang, D., Yu, A., and Chen, Z. (2018). Stringed "tube on cube" nanohybrids as compact cathode matrix for high-loading and lean-electrolyte lithium-sulfur batteries. *Energy Environ. Sci.* **11**, 2372–2381.
 43. Hou, T.-Z., Xu, W.-T., Chen, X., Peng, H.-J., Huang, J.-Q., and Zhang, Q. (2017). Lithium bond chemistry in lithium-sulfur batteries. *Angew. Chem. Int. Ed.* **56**, 8178–8182.
 44. Hwang, J., Rao, R.R., Giordano, L., Katayama, Y., Yu, Y., and Shao-Horn, Y. (2017). Perovskites in catalysis and electrocatalysis. *Science* **358**, 751.
 45. Liu, D., Zhang, C., Zhou, G., Lv, W., Ling, G., Zhi, L., and Yang, Q.-H. (2018). Catalytic effects in lithium-sulfur batteries: promoted sulfur transformation and reduced shuttle effect. *Adv. Sci.* **5**, 1700270.
 46. Yeon, J.S., Park, S.H., Suk, J., Lee, H., and Park, H.S. (2020). Confinement of sulfur in the micropores of honeycomb-like carbon derived from lignin for lithium-sulfur battery cathode. *Chem. Eng. J.* **382**, 122946.
 47. Luo, D., Deng, Y.-P., Wang, X., Li, G., Wu, J., Fu, J., Lei, W., Liang, R., Liu, Y., Ding, Y., et al. (2017). Tuning shell numbers of transition metal oxide hollow microspheres toward durable and superior lithium storage. *ACS Nano* **11**, 11521–11530.
 48. Chaneliere, C., Autran, J.L., Devine, R.A.B., and Bolland, B. (1998). Tantalum pentoxide (Ta₂O₅) thin films for advanced dielectric applications. *Mater. Sci. Eng. R Rep.* **22**, 269–322.